ELSEVIER

Comput. Methods Appl. Mech. Engrg. 157 (1998) 151–175

Computer methods in applied mechanics and engineering

Finite element computation of unsteady viscous compressible flows

S. Mittal

Department of Aerospace Engineering, Indian Institute of Technology, Kanpur, UP 208 016, India

Received 4 March 1996; revised 25 May 1997

Abstract

In this article we present our results for computation of unsteady viscous transonic flows past cylinders and airfoils. Stabilized finite element methods are employed to solve the compressible Navier–Stokes equations in their conservation law form. The nonlinear equations resulting from the finite element discretizations are solved using GMRES technique. To test the accuracy of the formulation, Mach 2 flow past a circular cylinder is computed with a mesh that is fine enough to resolve the shock structure for Reynolds number 50. The computational results agree quite well with the analytical and theoretical results. The methodology is applied to compute unsteady transonic flows past cylinders and airfoils. Several cases involving flows past a NACA0012 airfoil are computed and compared with numerical results from other researchers. Interesting flow patterns are observed for all the cases. It is observed that flow past an airfoil in a channel, of width 8.5 chord-lengths, at Mach 0.85 and Re 10 000 is unsteady when it is placed at zero incidence to the flow, while it reaches a steady-state when the angle of attack of the airfoil is 10°. © 1998 Elsevier Science S.A.

1. Introduction

With the advancement in computing technology, both in terms of hardware and high performance algorithms, it is quite conceivable that Computational Fluid Dynamics (CFD) will play an increasingly important role in the design and performance analysis of aerospace components. For example, it is now possible to compute transonic flow past an entire airplane on a parallel-vector supercomputer [1,2]. However, most of such compressible flow computations have been carried out for steady flows. Interestingly, extensive research effort has gone into the computation of unsteady incompressible flows [3,4].

Viscous transonic flows are associated with complex interactions between the boundary/shear layers and shock/expansion waves. In the transonic regime, the flows are quite sensitive to the free-stream Reynolds and Mach numbers; the boundary/shear layer behavior mainly depends on the Reynolds number while the shock/expansion wave behavior depends mainly on the Mach number [5,6]. A number of numerical studies have been devoted to the analyses of steady inviscid transonic flows [7–13]. Fewer studies have been conducted for unsteady for unsteady, viscous flows [14–16]. In this article, we present our results for the computation of unsteady viscous transonic flows past airfoils and circular cylinders.

We begin by reviewing the governing equations in Section 2. The equations are written in the conservation law form. The stabilized variational formulation of these equations in terms of the conservation variables is presented in Section 3. The SUPG (streamline-upwind/Petrov–Galerkin) stabilization technique is employed to stabilize our computations against spurious numerical oscillations due to advection dominated flows. The SUPG technique was first introduced by Hughes and Brooks [17] for the advection–diffusion equation and for incompressible flows. It was introduced in the context of inviscid compressible flows by Tezduyar and Hughes [12,18] and Hughes and Tezduyar [7]. In addition to the SUPG stabilizations, we supplement our formulation with a shock-capturing term to provide stability of the computations in the presence of discontinuities and large gradients in the flow. The idea, in the context of conservation variables, was demonstrated by Le Beau and Tezduyar [11]. In the current work we employ the same shock capturing operator as the one by Le Beau and Tezduyar [11] but with a modified coefficient to account for the unsteadiness in the flow. We also demonstrate,

PII S0045-7825(97)00225-9

in Section 4 through a numerical example for unsteady flow past a NACA0012 airfoil, the effect of this modified term. In Section 4 we present our results for computation of flows past cylinders and airfoils. We begin with the computation of supersonic flow past a cylinder at Mach 2 and Re 50. The shock thickness is compared to the experimental and analytical results from other researchers. The effect of the shock capturing operator on the computed results is also studied. The robustness of the algorithm is demonstrated via a flow computation at Re 2000. Next, unsteady transonic flow past a cylinder at Mach 0.7 and Re 2000 is computed. To establish more confidence in the present implementation, our results for Mach 0.5 flow past a NACA0012 airfoil at Re 5000 is compared with those computed by Venkatakrishnan [19]. Computations are also presented for Mach 0.85 flow past a NACA0012 airfoil at Re 500, 2000 and 10 000 and zero incidence. From our computations we observe a steady flow for Re 2000 and an unsteady flow for Re 10 000. Interestingly, at Re 10 000 we again observe a steady flow when the airfoil is placed at a 10° incidence to the flow. Our preliminary results indicate this to be an effect of the placement of lateral boundaries. More details on this issue will be reported in a later article.

2. The governing equations

Let $\Omega \subset \mathbb{R}^{n_{sd}}$ and $(0, T)$ be the spatial and temporal domains respectivly, where n_{sd} is the number of space dimensions, and let Γ denote the boundary of Ω. The spatial and temporal coordinates are denoted by x and t. The Navier–Stokes equations governing the fluid flow, in conservation form, are

$$\frac{\partial \rho}{\partial t} + \nabla \cdot (\rho \boldsymbol{u}) = 0 \quad \text{on } \Omega \text{ for } (0, T), \tag{1}$$

$$\frac{\partial (\rho \boldsymbol{u})}{\partial t} + \nabla \cdot (\rho \boldsymbol{u}\boldsymbol{u}) + \nabla p - \nabla \cdot \boldsymbol{T} = \boldsymbol{0} \quad \text{on } \Omega \text{ for } (0, T), \tag{2}$$

$$\frac{\partial (\rho e)}{\partial t} + \nabla \cdot (\rho e \boldsymbol{u}) + \nabla \cdot (p \boldsymbol{u}) - \nabla \cdot (\boldsymbol{T}\boldsymbol{u}) + \nabla \boldsymbol{q} = 0 \quad \text{on } \Omega \text{ for } (0, T) \tag{3}$$

Here, ρ, $\boldsymbol{u}$, p, $\boldsymbol{T}$, e and $\boldsymbol{q}$ are the density, velocity, pressure, viscous stress tensor, the total energy per unit mass, and the heat flux vector, respectively. The viscous stress tensor is defined as

$$\boldsymbol{T} = \mu((\nabla \boldsymbol{u}) + (\nabla \boldsymbol{u})^{\mathrm{T}}) + \lambda(\nabla \cdot \boldsymbol{u})\boldsymbol{I}. \tag{4}$$

where μ and λ are the viscosity coefficients. It is assumed that μ and λ are related by

$$\lambda = -\frac{2}{3}\mu. \tag{5}$$

Pressure is related to the other variables via the equation of state. For ideal gases, the equation of state assumes the special form

$$p = (\gamma - 1)\rho i, \tag{6}$$

where γ is the ratio of specific heats and i is the internal energy per unit mass that is related to the total energy per unit mass and velocity as

$$i = e - \frac{1}{2}\|\boldsymbol{u}\|^2. \tag{7}$$

The heat flux vector is defined as

$$\boldsymbol{q} = -\kappa \nabla \theta, \tag{8}$$

where κ is the heat conductivity and θ is the temperature. The temperature related to the internal energy by the following relation

$$\theta = \frac{i(\gamma - 1)}{R} \tag{9}$$

where R is the ideal gas constant. Prandtl number (P_r), assumed to be specified, relates the heat conductivity to the fluid viscosity according to the following relation

$$\kappa = \frac{\gamma R \mu}{(\gamma - 1) P_r} \tag{10}$$

The compressible Navier–Stokes equations (1), (2) and (3) can be written in the conservation variables

$$\frac{\partial U}{\partial t} + \frac{\partial F_i}{\partial x_i} - \frac{\partial E_i}{\partial x_i} = 0 \quad \text{on } \Omega \text{ for } (0, T), \tag{11}$$

where $U = (\rho, \rho u_1, \rho u_2, \rho e)$, is the vector of conservation variables, and F_i and E_i are, respectively, the Euler and viscous flux vectors defined as

$$F_i = \begin{pmatrix} u_i \rho \\ u_i \rho u_1 + \delta_{i1} p \\ u_i \rho u_2 + \delta_{i2} p \\ u_i (\rho e + p) \end{pmatrix},$$

$$E_i = \begin{pmatrix} 0 \\ \tau_{i1} \\ \tau_{i2} \\ -q_i + \tau_{ik} u_k \end{pmatrix} \tag{13}$$

Here, u_i, q_i and τ_{ik} are the components of the velocity, heat flux and viscous stress tensor, respectively. In the quasi-linear form, Eq. (11) is written as

$$\frac{\partial U}{\partial t} + A_i \frac{\partial U}{\partial x_i} - \frac{\partial}{\partial x_i}\left(K_{ij} \frac{\partial U}{\partial x_j} \right) = 0 \quad \text{on } \Omega \text{ for } (0, T), \tag{14}$$

where

$$A_i = \frac{\partial F_i}{\partial U},$$

is the Euler Jacobian Matrix, and K_{ij} is the diffusivity matrix satisfying

$$K_{ij} \frac{\partial U}{\partial x_j} = E_i$$

Corresponding to Eq. (14), the following boundary and initial conditions are chosen

$$U = g \quad \text{on } \Gamma_g \text{ for } (0, T),$$

$$n \cdot E = h \quad \text{on } \Gamma_h \text{ for } (0, T),$$

$$U(x, 0) = U_0 \quad \text{on } \Omega_0$$

3. Finite element formulation

Consider a finite element discretization of Ω into subdomains Ω^e, $e = 1, 2, \ldots, n_{el}$, where n_{el} is the number of elements. Based on this discretization, we define the finite element trial function space $\mathcal{S}^h$ and weighting function space $\mathcal{V}^h$. These function spaces are selected, by taking the Dirichlet boundary conditions into account, as subsets of $[H^{1h}(\Omega)]^{n_{dof}}$, where $H^{1h}(\Omega)$ is the finite-dimensional function space over Ω and n_{dof} is the number of degrees of freedom.

$$\mathcal{S}^h = \{U^h \mid U^h \in [H^{1h}(\omega)]^{n_{dof}}, \quad U^h|_{\Omega^e} \in [P^1(\Omega^e)]^{n_{dof}}, \quad U^h \cdot e_k \doteq g_k \text{ on } \Gamma_{g_k}\}, \tag{20}$$

$$\mathcal{V}^h = \{W^h \mid W^h \in [H^{1h}(\Omega)]^{n_{dof}}, \quad W^h|_{\Omega^e} \in [P^1(\Omega)^e)]^{n_{dof}}, \quad W^h \cdot e_k \doteq 0 \text{ on } \Gamma_{g_k}\}$$

where $[P^1(\Omega^e)]$ represents the first-order polynomial in Ω^e, and $k = 1, \ldots, n_{dof}$. The stabilized finite element formulation of Eq. (14) is written as follows: find $U^h \in \mathcal{S}^h$ such that $\in W^h \in \mathcal{V}^h$.

$$\int_\Omega W^h \cdot \left(\frac{\partial U^h}{\partial t} + A_i^h \frac{\partial U^h}{\partial x_i}\right) \mathrm{d}\Omega + \int_\Omega \left(\frac{\partial W^h}{\partial x_i}\right) \cdot \left(K_{ij}^h \frac{\partial U^h}{\partial x_j}\right) \mathrm{d}\Omega$$
$$+ \sum_{e=1}^{n_{el}} \int_{\Omega^e} \tau (A_k^h)^T \left(\frac{\partial W^h}{\partial x_k}\right) \cdot \left[\frac{\partial U^h}{\partial t} + A_i^h \frac{\partial U^h}{\partial x_i} - \frac{\partial}{\partial x_i}\left(K_{ij}^h \frac{\partial U^h}{\partial x_j}\right)\right] \mathrm{d}\Omega$$
$$+ \sum_{e=1}^{n_{el}} \int_{\Omega^e} \delta \left(\frac{\partial W^h}{\partial x_i}\right) \left(\frac{\partial U^h}{\partial x_i}\right) \mathrm{d}\Omega = \int_{\Gamma_h} W^h \cdot h^h \, \mathrm{d}\Gamma$$

REMARKS

(1) In the variational formulation given by Eq. (22), the first two terms and the right-hand side constitute the Galerkin formulation of the problem.

(2) The first series of element-level integrals in Eq. (22) are the SUPG stabilization terms added to the variational formulation to stabilize the computations against node-to-node oscillations in the advection-dominated range. The second series of element level integrals in the formulation are the shock-capturing terms that stabilize the computations in the presence of sharp gradients. The stabilization coefficients δ and τ are quite similar to the ones that are used by Le Beau [10] and Le Beau et al. [11] and are defined as

$$\tau = \max[0, \tau_a - \tau_\delta],$$

$$\tau_a = \left(\left(\frac{2(c + \|u\|)}{h}\right)^2 + \left(\frac{12\nu}{h^2}\right)^2\right)^{-1/2}$$

$$\tau_\delta = \frac{\delta}{2(c + \|u\|)^2} I$$

$$\delta = \left[\frac{\left\| \frac{\partial U}{\partial t} + A_i \frac{\partial U}{\partial x_i} \right\|_{A_0^{-1}}}{\left\| J_{1i} \frac{\partial U}{\partial x_i} \right\|_{A_0^{-1}} + \left\| J_{2i} \frac{\partial U}{\partial x_i} \right\|_{A_0^{-1}}} \right]^1$$

where c is the wave speed, h is the element length, J_{jk} are the components of Jacobian transformation matrix from physical to the local coordinates and A_0^{-1} is the inverse of Reimannian metric tensor [20]. This definition of τ_a is based on a simple multi-dimensional generalization of the optimal one given by Shakib [21] for one-dimensional space–time formulation. A similar definition has also been used, extensively, for computation of incompressible flows [3,4,22]. The element length h is defined as

$$h = 2\left(\sum_{a=1}^{n_{en}} |s \cdot \nabla N_a|\right)$$

where N_a is the basis function associated with the node a, n_{en} is the number of nodes in the element, and s is the unit vector in the direction of the local velocity. Matrix τ_δ is subtracted from τ_a to account for the shock-capturing term as shown in Eq. (23). The definition of δ used in Eq. (26) is the same as in [1,10,11,23] except that it includes the unsteady term in the numerator that renders consistency to the formulation, even for unsteady computations. It has been our experience that in some cases, if the unsteady term is not included in the definition of δ, one may obtain overly damped solutions for unsteady flow problems. For e.g. in the computation of unsteady flow past a NACA0012 airfoil at Re 10 000 and zero incidence, the exclusion of the unsteady term in Eq. (26) alters the vortex shedding, significantly. Of course, for steady computations, this term does not affect the final solution. In fact, one would like to drop this term to gain extra stability to converge to the final solution.

(3) The time discretization of the variational formulation given by Eq. (22) is done via the generalized trapezoidal rule. For unsteady computations, we employ a second-order accurate-in-time procedure.

4. Numerical Simulations

All the computations reported in this article are carried out on work-stations (Digital 3000/600 and 3000/300 AXP) at IIT Kanpur. The nonlinear equation systems resulting from the finite-element discretization of the flow equations are solved using the Generalized Minimal RESidual (GMRES) technique [24] in conjunction with block-diagonal preconditioners. The Prandtl Number for all the cases in 0.72. Unless explicitly stated, the viscosity of the fluid is assumed to be constant in the entire domain.

4.1. Mach 2 flow past a cylinder

The aim of this computation is to establish confidence in our formulation and its implementation. The mesh employed, consisting of 16 000 quadrilateral elements and 16 200 nodes, is shown in Fig. 1. The Reynolds number is based on the diameter of the cylinder and the free-stream values of the velocity and kinematic

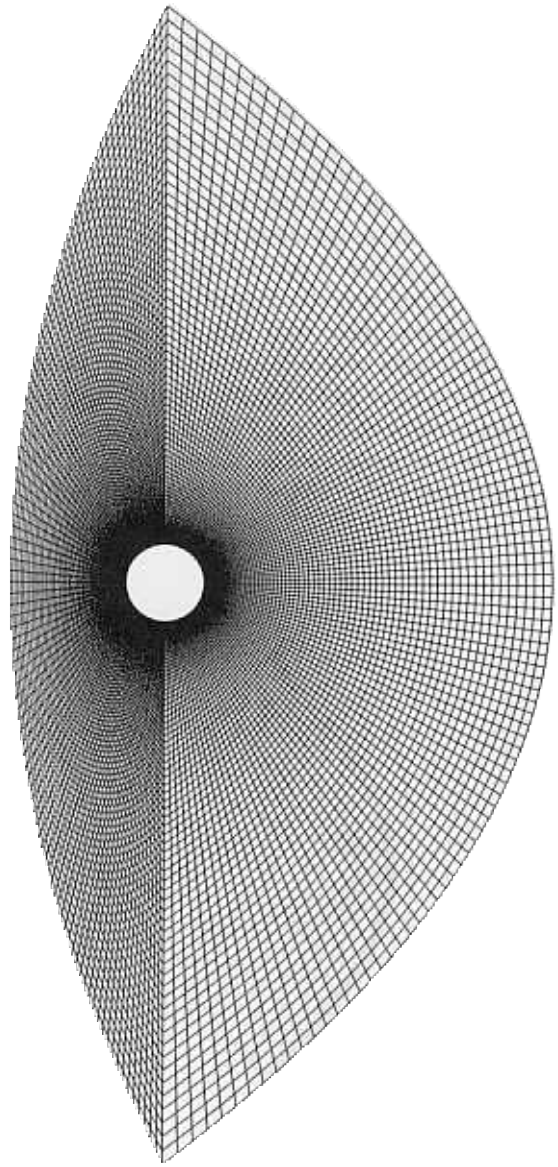

Fig. 1. Mach = 2 flow past a cylinder: the finite element mesh; number of nodes = 16 200 and number of elements = 16 000.

viscosity. The cylinder wall is assumed to be adiabatic and the no-slip condition is specified for the velocity on the surface of the cylinder. All the variables are specified on the upstream boundary. At the downstream boundary, we specify a neumann type boundary condition for the velocity and energy that correspond to zero viscous stress and heat flux vectors. The computations are initiated with free-stream conditions in the entire domain and continue till the steady-state norm of the solution falls below a certain desired value.

We first carry out the computation at Re 50. At this low Reynolds number, our mesh is fine enough to resolve all the gradients in the flow. Therefore, the shock-capturing operator is turned off. Reported in [25] are analytical results for the shock thickness at various Mach and Reynolds numbers. These results are calculated by assuming a viscosity–temperature relationship of the form $\mu \sim \theta^{0.768}$ and agree quite well with measurements in experiments involving flow of air. To compare our computational results with the above-mentioned results we carry out the computations with the same viscosity–temperature relationship. From our computed results we find that the shock-Reynolds number (based on the shock-thickness and the free-stream values of density, speed of sound and dynamic viscosity) is 4.4. Shapiro [25] reports the value of this shock-Reynolds number to be 4.6. Fig. 2 shows the density, pressure and Mach number fields for the computed solution after it attains a steady-state. Next, we turn on the shock capturing operator to see its effect on the solution. Fig. 3 shows the density, pressure and Mach number fields for the computed solution with the shock-capturing operator turned on. We observe that this solution looks similar to the one in the previous case (with the shock capturing operator turned off). The solution computed with shock capturing operator turned on is relatively a little more diffused in the regions of high gradients. In the regions where the gradients in the solution are not too significant, the solutions are quite indistinguishable. This is a very desirable feature of a good shock capturing operator and confirms the accuracy and consistency of our formulation.

Next, we carry out the computation at Re 2000. It should be noted, that at Re 2000, the shock is quite thin and one would need an extremely fine mesh to resolve the shock structure. Therefore, this case is computed with the shock-capturing operator turned on. Shown in Fig. 4 are the density, pressure and Mach number fields for the steady-state solution. One can observe a strong bow shock upstream of the cylinder and a weak tail shock in the wake. The shock stand-off distance compares quite well with experimental observations [26]. It can also be observed that the shock has been captured quite well within two to three elements. Fig. 5 shows the distribution of the pressure coefficient on the cylinder surface and along the plane of symmetry of the computational domain. On comparing the solutions at Reynolds numbers 50 and 2000 we observe that, as expected, the gradients are much larger for the Re 2000 case. For example, the tail shock which is extremely weak at Re 50 is quite prominent at Re 2000. The drag coefficient at Re 2000 is 1.44 while it is 1.9 at Re 50.

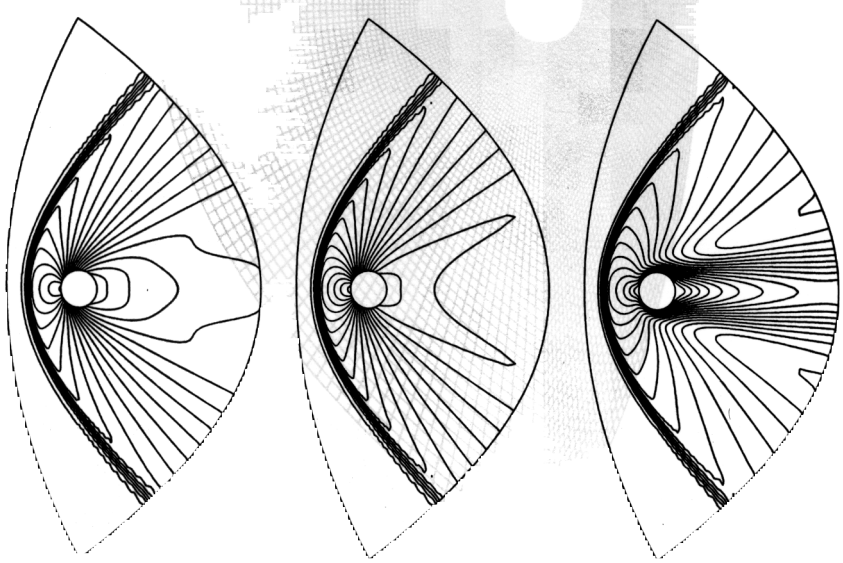

Fig. 2. Mach = 2, Re = 50 flow past a cylinder computed without the shock-capturing operator: density, pressure and Mach number fields for the steady state solution.

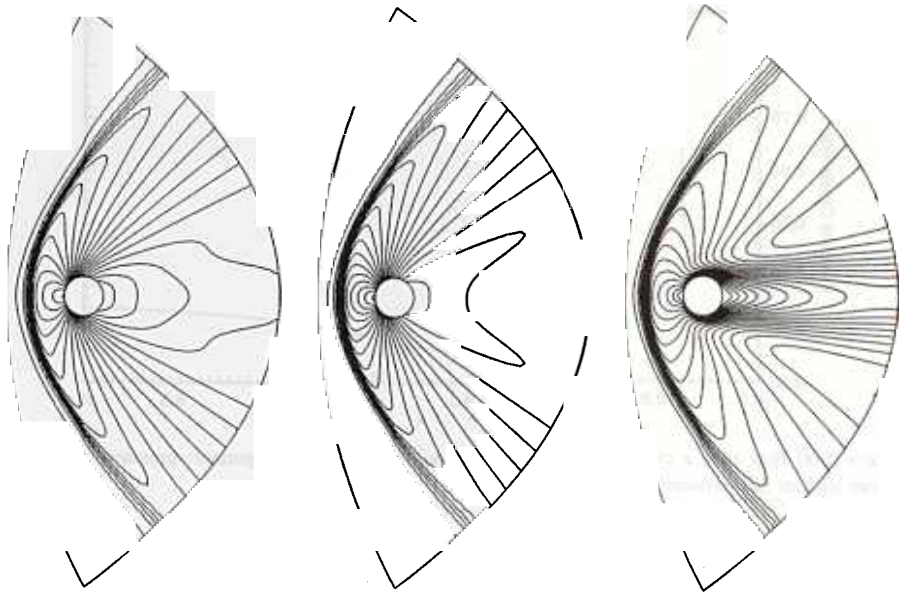

Fig. 3. Mach = 2, Re = 50 flow past a cylinder computed with the shock-capturing operator: density, pressure and Mach number fields for the steady state solution.

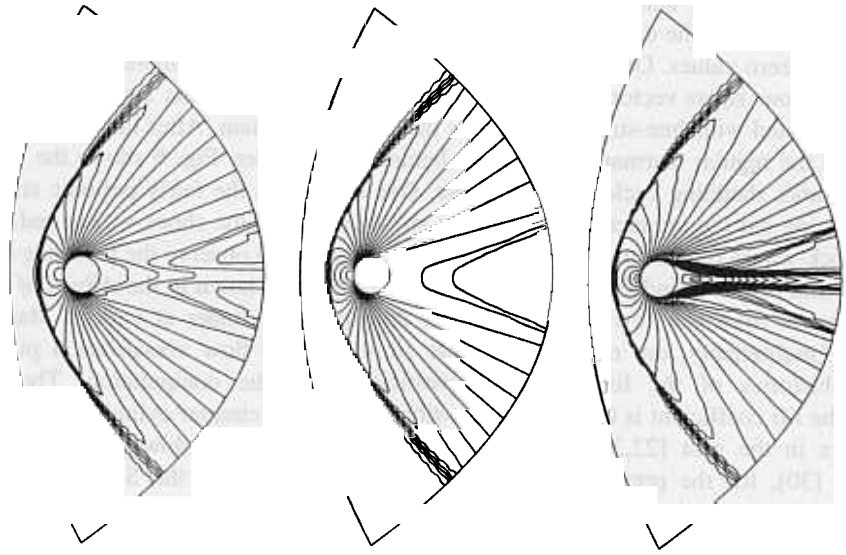

Fig. 4. Mach = 2, Re = 2000 flow past a cylinder computed with the shock-capturing operator: density, pressure and Mach number fields for the steady state solution.

4.2. Mach 0.7, Re 2000 flow past a cylinder

Having established confidence in our computations for certain simple flows, we present our computations for more complex transonic flows that are unsteady and involve shock-boundary layer interactions. In this section we present our solutions for flow past a circular cylinder at Re 2000 and Mach 0.7. The cylinder resides in a rectangular computational domain whose upstream and downstream boundaries are located at 15 and 45 cylinder radii, respectively, from the cylinder's center. The upper and lower boundaries are placed at 15 radii from the center of the cylinder. The finite element mesh consists of 17 108 quadrilateral elements and 17 434 nodes. At each time step, 68 693 nonlinear equations are solved iteratively to compute the flow field. The issue of

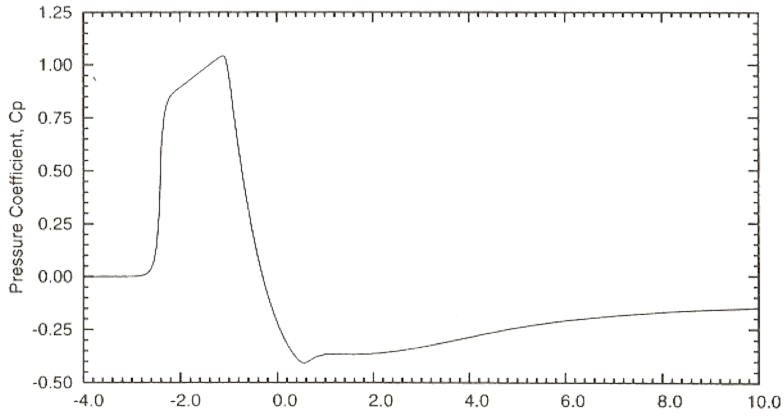

Fig. 5. Mach = 2, Re = 2000 flow past a cylinder computed with the shock-capturing operator: pressure coefficient along the line of symmetry. The cylinder surface lies between $x = -1$ and $x = 1$.

imposing the right set of boundary conditions for the compressible Navier–Stokes equations is fairly complicated and has been addressed by several researchers in the past. The interested readers referred to the work by Oliger and Sundstrom [27] and Gustafsson and Sundstrom [28]. In our computations the cylinder surface is assumed to be adiabatic and the no-slip condition is specified for the velocity on the cylinder wall. At the upstream boundary, density and both components of velocity are assinged free-stream values and the heat flux is assumed to be zero. At the downstream boundary, we prescribe the pressure while the viscous stress and heat flux are assigned zero values. On the upper and lower boundaries, the component of velocity normal to and the component of viscous stress vector along these boundaries and the heat flux are prescribed zero values. The computations are initiated with free-stream conditions in the entire domain. After the initial transience, one sees the development of the regular Karman Vortex sheet behind the cylinder. Fig. 6 shows the density field at five instants during a vortex shedding cycle of the cylinder. One can notice the fairly periodic structure in the flow. The pictures also bring out the interaction between the shear-layer, and the shock-waves and expansion fans. In addition to the shock-waves on the surface of the cylinder, one can also observe the presence of shock-waves, in the wake, downstream of the cylinder that destabilize the shear layer. Shown in the *Album of Fluid Motion* [29] are a few photographs from the flow visualization for flow past a cylinder at various Mach numbers in the transonic regime. Qualitatively, our results look quite similar to the flow visualization pictures [29]. Fig. 7 shows the time histories of the lift and drag coefficients for the computation. The Strouhal number corresponding to the lift coefficient is 0.17. Incompressible flow past a circular cylinder has been investigated by various researchers in the past [22,30]. Compared to the incompressible flow past a cylinder at the same Reynolds number [30], for the present case we observe lower values of the Strouhal number and the lift coefficient amplitude, and a higher value of the drag coefficient. For incompressible flow, past a cylinder at Re 2000, Behr [30] reports the Strouhal number, amplitude of lift coefficient and the mean drag coefficient, respectively, to be 0.244, 1.7 and 1.6. They have also observed that unlike the flow at Re 1000, for the flow at Re 2000 the vortex street oscillates about the centerline of the domain. Shown in Fig. 8 are the pressure, entropy, vorticity, Mach number, and supersonic Mach number fields corresponding to the minimum value of the lift coefficient for the periodic solution.

4.3. Mach = 0.5, Re = 5000, $\alpha = 0°$ flow past a NACA0012 airfoil

A NACA0012 airfoil is placed in a Mach 0.5 flow. The Reynolds number is based on the chord of the airfoil and the free-stream velocity and kinematic viscosity. The mesh employed consists of 18 772 quadrilateral elements and 19 014 nodes. The upstream and down stream boundaries are located at 4.25 and 7.75 chord-lengths, respectively, with respect to the mid-chord point of the airfoil. The upper and lower boundaries are 4.25 chord lengths away, each, from the mid-point of the airfoil. The finite element mesh, employed for computations in this article, is shown in Fig. 9. The boundary conditions for this problem are specified in the

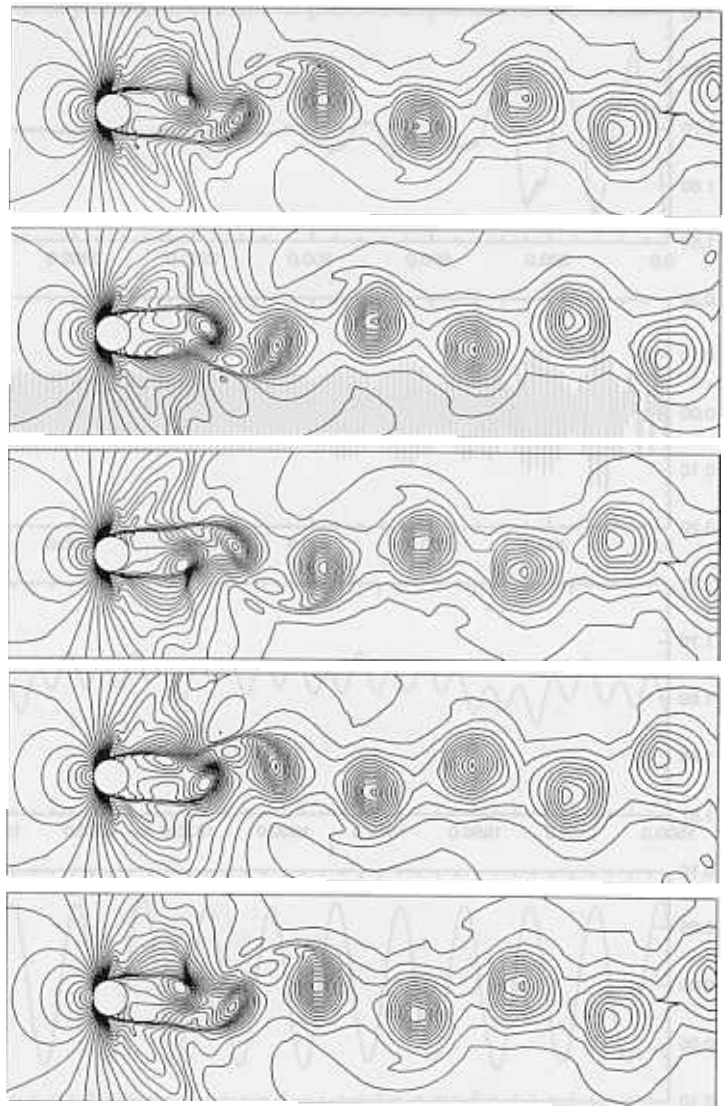

Fig. 6. Mach = 0.7, Re = 2000 flow past a cylinder: density field at five instants during one vortex shedding cycle.

same way as for the transonic flow past a circular cylinder (in the previous section). The computations are initiated with free-stream conditions in the entire domain. These results are calculated by assuming a viscosity-temperature relationship of the form $\mu \sim \theta^{0.768}$.

Fig. 10 shows the steady-state solution for this problem. Shown in Figs. 11 and 12 are the chord-wise distribution of the pressure and skin friction coefficients from the present computations and from other researchers [19]. It can be observed that the agreement betwen the two sets of results is excellent. Compared to the peak value of the skin friction coefficient at the nose reported in [19], our calculations result in a slightly lower value. This is perhaps because the mesh that we have employed is not sufficiently refined near the nose of the airfoil for this Reynolds Number and it is well known that the peak value of C_f is quite sensitive to the refinement of the mesh near the leading edge of the airfoil. The drag coefficient from the present calculations is 0.55. The same value is reported by Venkatkrishnan [19]. The separation point, from the present computations, is located at 81.3% of the chord from the leading edge. Venkatkrishnan [19] reports this value to be in the range of 81.0–82.4% for the various grids they employed. For the finest grid, they used, the separation point is located at 81.4% of the chord from the leading edge.

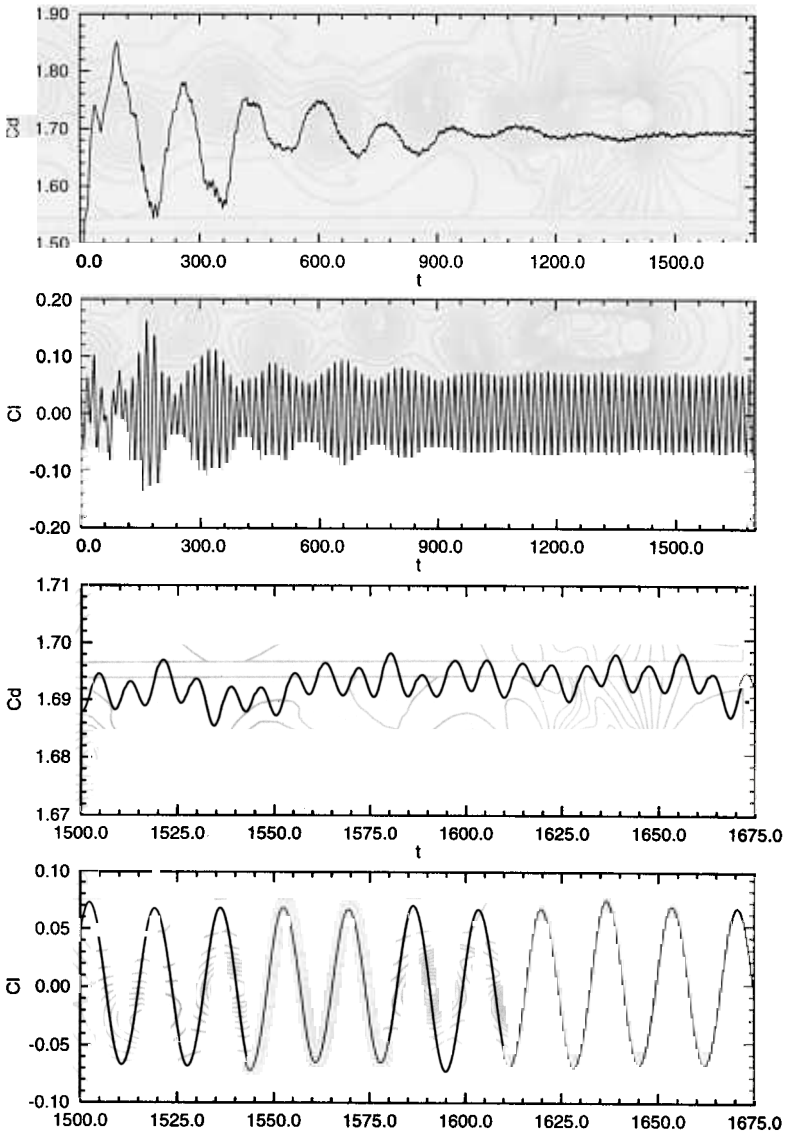

Fig. 7. Mach = 0.7, Re = 2000 flow past a cylinder: time histories of the lift and drag coefficients.

4.4. Mach 0.85 flow past a NACA0012 airfoil

A NACA0012 airfoil is placed in a Mach 0.85 flow. The mesh employed is the same as described in the previous section.

4.4.1. Re = 500, $\alpha = 0°$

This is one of the standard test cases reported in one of the GAMM workshops [14,31]. The boundary conditions for this case are the same as reported in previous section except that on the airfoil surface a free-stream total temperature, T_0 is specified:

$$T_0 = T_\infty\left(1+\frac{\gamma-1}{2}M_\infty^2\right) \tag{28}$$

where T_∞ and M_∞ are, respectively, the free-stream temperature and Mach number. Fig. 13 shows the pressure, entropy and Mach number fields for the steady-state solution to this problem. Shown in Figs. 14 and 15 are the

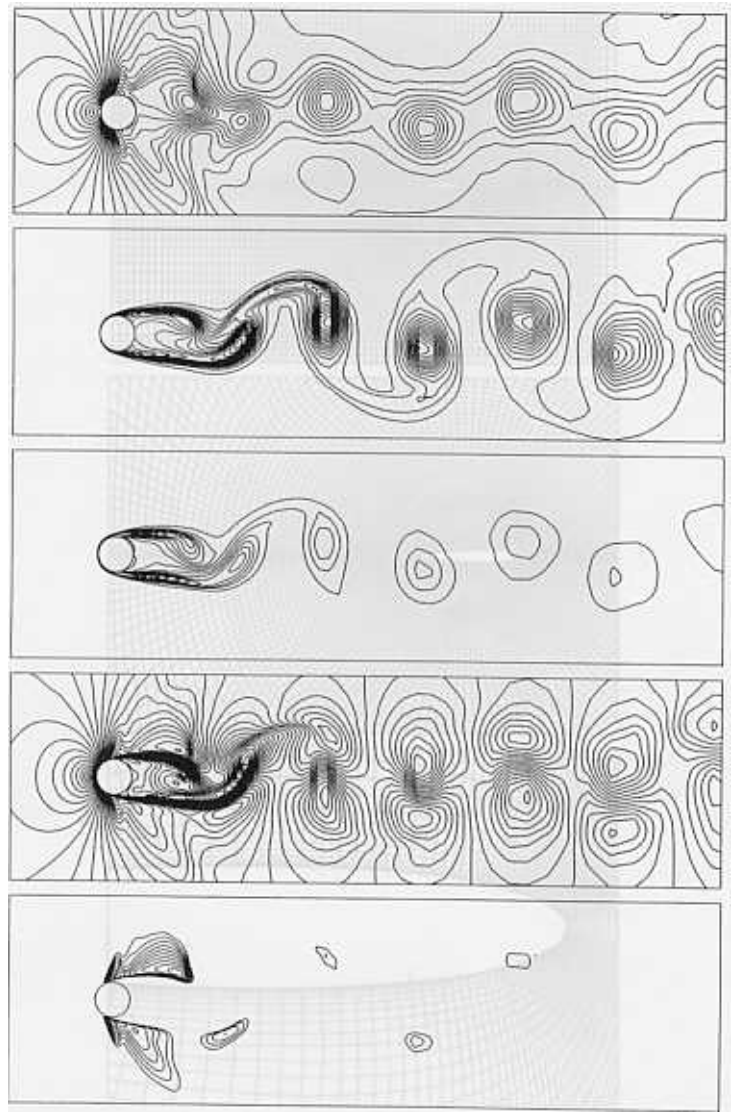

Fig. 8. Mach = 0.7, Re = 2000 flow past a cylinder: pressure, entropy, vorticity, Mach number and supersonic Mach number fields corresponding to the minimum value of the lift coefficient.

chord-wise distribution of the pressure and skin friction coefficients from the present computations and from other researchers [32–35]. Muller et al. [32] have carried out the computations by means of an implicit central difference scheme due to Beam and Warming using a 193×65 grid. Shakib et al. [33] have reported the results for this problem with three unstructured nested meshes, consisting of 801, 3118 and 12 300 nodes and have employed a finite element formulation based on entropy variables. However, they remark that even their finest grid may not be enough to resolve the boundary layer. Results from Shakib et al. [33], shown in Figs. 14 and 15, are for their finest mesh. Cambier [34] has reported results for this problem using MacCormack's finite difference scheme in conjunction with an explicit predictor–corrector algorithm on a 193×47 grid. Satofuka et al. [35] have utilized the method of lines for spatial discretization and an explicit rational Runge–Kutta method for time integration to conmpute this problem with a 257×65 grid. It can be observed that the C_f distribution from the present computations matches quite well with the one reported by Shakib et al. [33] for their finest mesh. However, the match with results from other researchers is not too good. We have also carried out this computation on a finer mesh with 34 694 nodes and 34 292 quadrilateral elements. The results are almost indistinguishable from the present ones except for the C_f value near the nose of the airfoil. The refined mesh

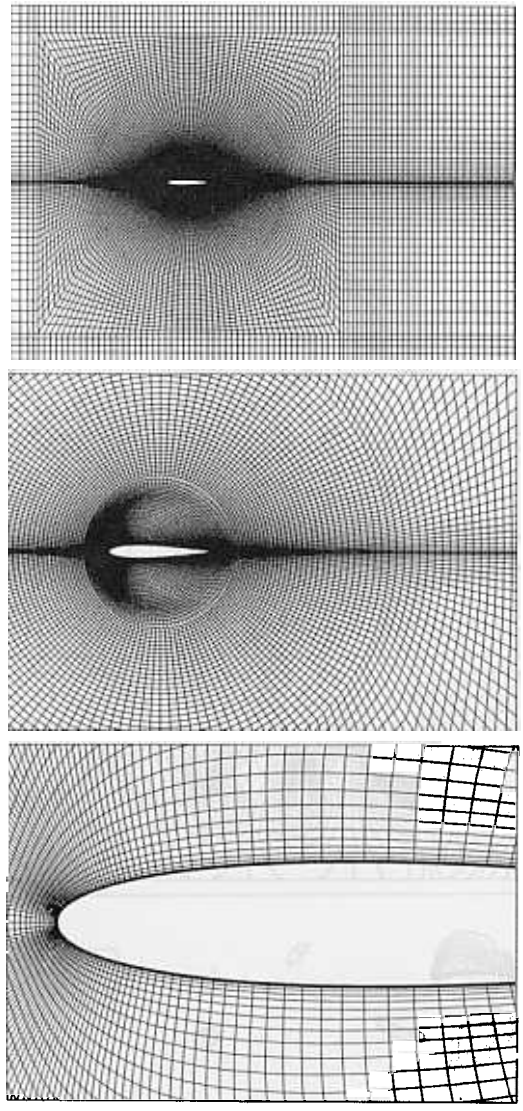

Fig. 9. Flow past a NACA0012 airfoil: the finite element mesh; number of nodes = 19 014 and number of elements = 18 772.

results in a slightly higher value of C_f at the nose, as expected. From the plot of the C_p distribution it can be seen that the values from the present computations lie somewhere in between the values reported by Shakib et al. [33] for the finest grid and those reported by other researchers. The discrepancy in the various results can perhaps be explained by the difference in the predicted location of the shock for calculations by various researchers which can be observed from the contour plots (in the respective references). The method that is being used here and the one used by Shakib et al. [33] have been vigorously tested on many problems and have led to very satisfactory results. It has been well established that these methods result in the correct location and strength of shocks in the flows [1,2,10,11,16,20,21,23]. The steady state drag coefficient from the present computations is 0.259. The values reported by various reserchers in the GAMM workshop [14] lie in the range 0.096–0.242. Shakib et al. [33] have not reported the drag coefficient for their computation.

4.4.2. $Re = 2000$, $\alpha = 0°$

This is another test problem in one of the GAMM workshops [14,15]. The boundary conditions are the same as in the previous section. Shown in Fig. 16 are the pressure, entropy and Mach number fields for the steady-state solution. The steady-state drag coefficients is 0.153. The values reported by other researchers [14]

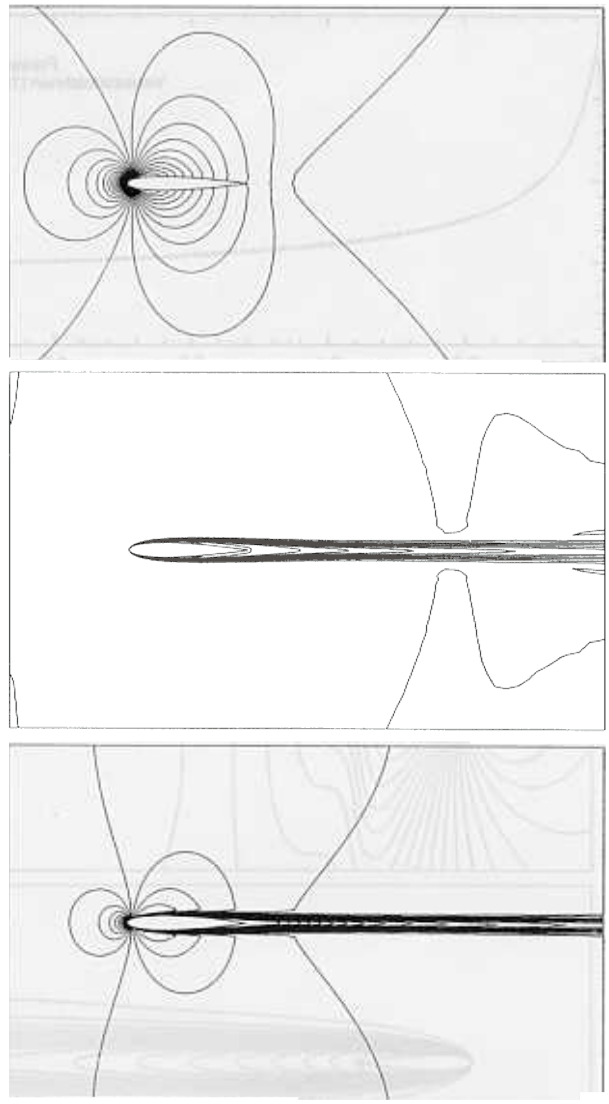

Fig. 10. Mach = 0.5, Re = 5000, $\alpha = 0°$ flow past a NACA0012 airfoil: pressure, entropy and Mach number (top to bottom) for the steady state solution.

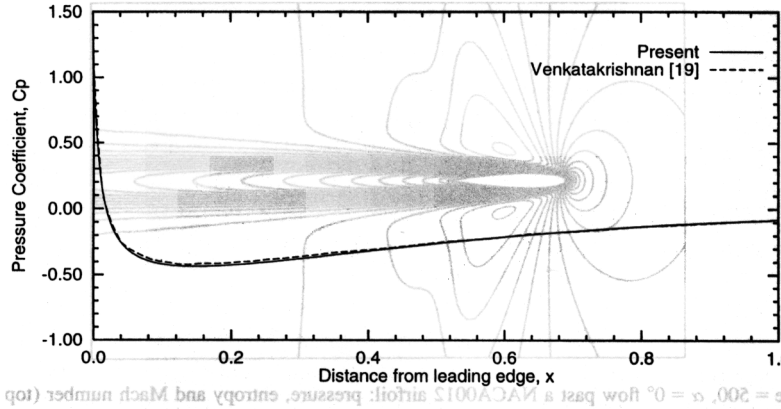

Fig. 11. Mach = 0.5, Re = 5000, $\alpha = 0°$ flow past a NACA0012 airfoil: chord-wise variation of the pressure coefficient.

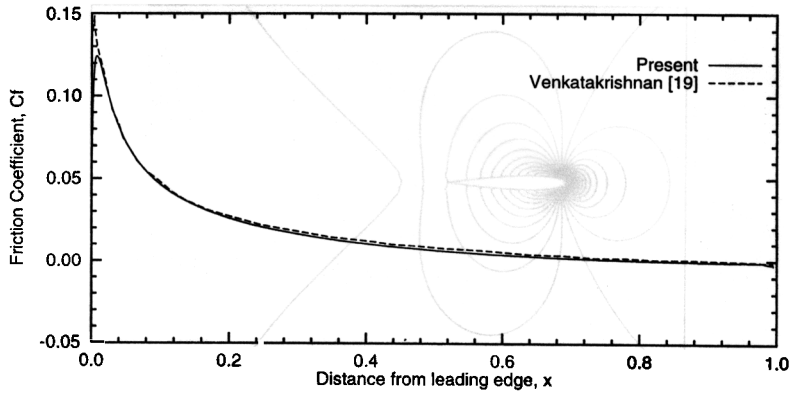

Fig. 12. Mach = 0.5, Re = 5000, $\alpha = 0°$ flow past a NACA0012 airfoil: chord-wise variation of the skin-friction coefficient.

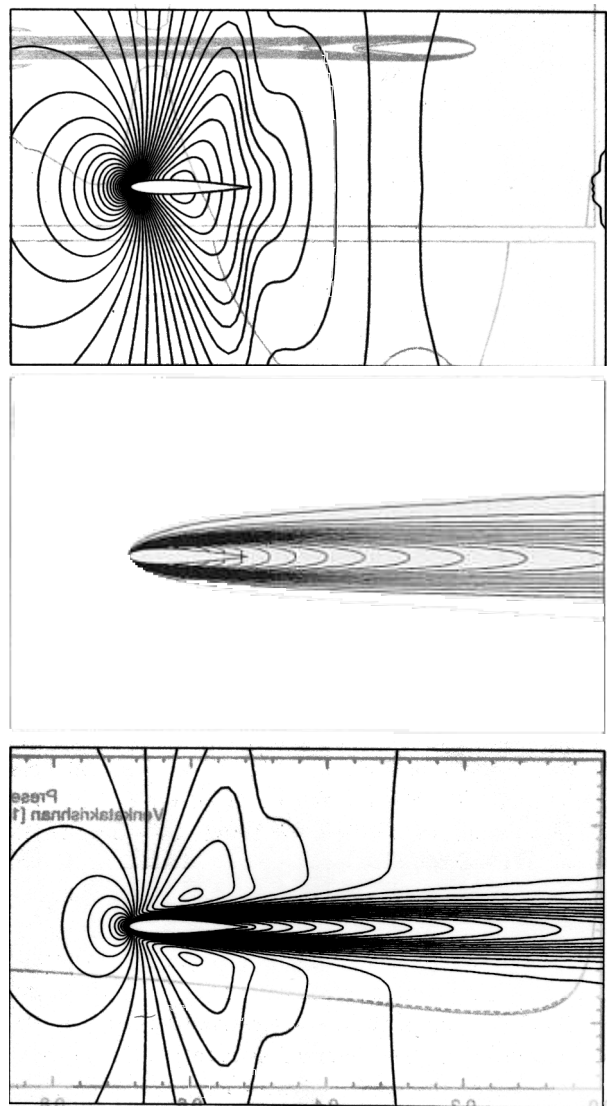

Fig. 13. Mach = 0.85, Re = 500, $\alpha = 0°$ flow past a NACA0012 airfoil: pressure, entropy and Mach number (top to bottom) for the steady state solution.

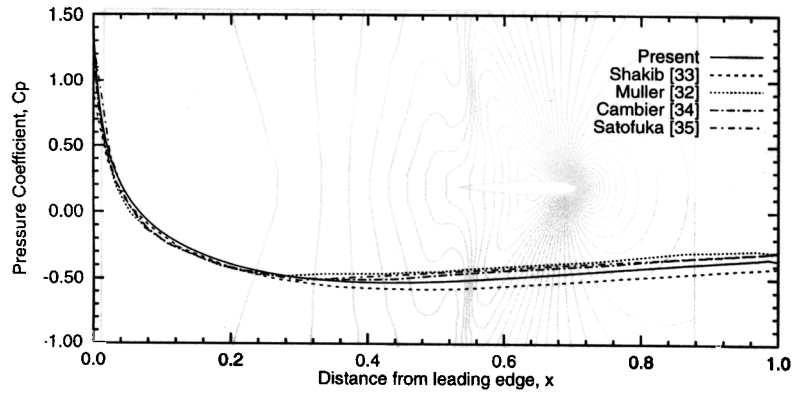

Fig. 14. Mach = 0.85, Re = 500, $\alpha = 0°$ flow past a NACA0012 airfoil: chord-wise variation of the pressure coefficient.

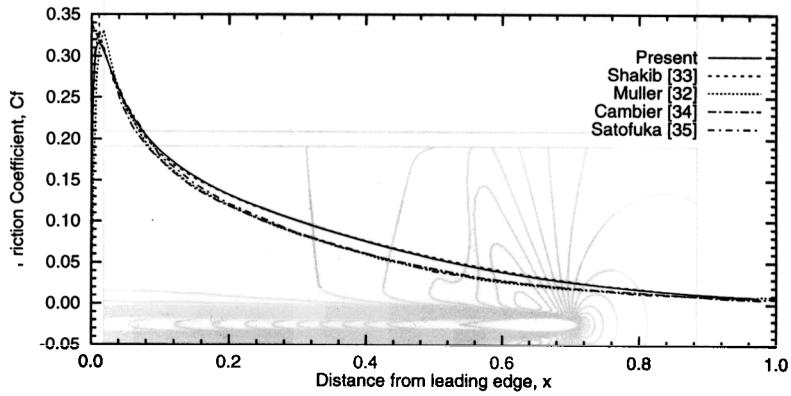

Fig. 15. Mach = 0.85, Re = 500, $\alpha = 0°$ flow past a NACA0012 airfoil: chord-wise variation of the skin-friction coefficient.

lie in the range 0.101–0.136. Shown in Figs. 17 and 18 are the chord-wise distribution of the pressure and skin friction coefficients from the present computations and from other researchers [34,35]. On comparing the contour plots for the present solution with the ones from Satofuka et al. [35] we observe that the locations of shock are quite different. This also explains the difference between the drag coefficients and the C_p distribution for the two calculations.

4.4.3. Re = 10 000, $\alpha = 0°$

At Reynolds number 10 000 our computations result in an unsteady solution. The boundary conditions for computations in this section and in the remaining article are the same as for circular cylinder, described earlier. After the initial transience, a fully developed periodic solution is observed. Fig. 19 shows the density field at five instants during one cycle of lift coefficient. The interaction between the shock and expansion waves, and the boundary and shear layers can be clearly observed. Downstream of the front stagnation point, the flow expands until it reaches, approximately, the mid-chord point. By this point, the boundary layer thickness increases causing the flow to constrict resulting in the formation of a weak oblique shock. The interaction between the

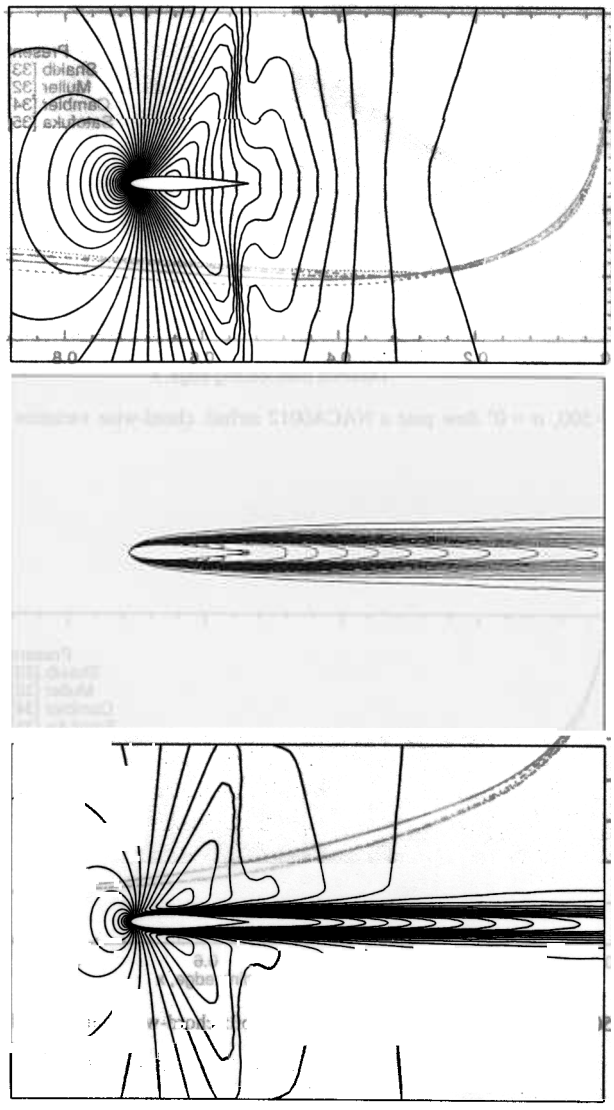

Fig. 16. Mach = 0.85, Re = 2000, $\alpha = 0°$ flow past a NACA0012 airfoil: pressure, entropy and Mach number fields (top to bottom) for the steady state solution.

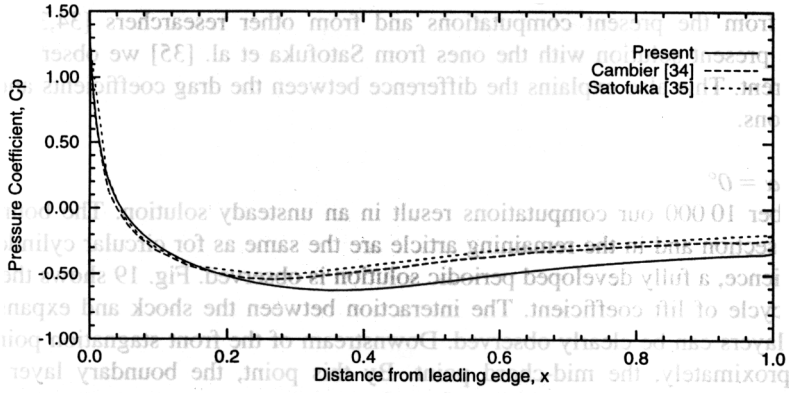

Fig. 17. Mach = 0.85, Re = 2000, $\alpha = 0°$ flow past a NACA0012 airfoil: chord-wise variation of the pressure coefficient.

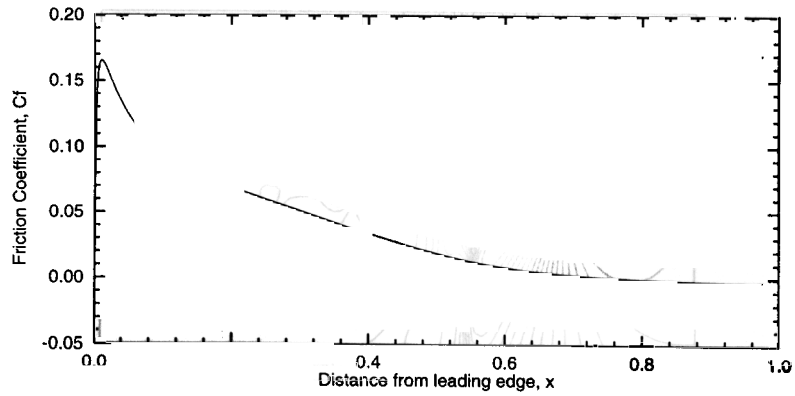

Fig. 18. Mach = 0.85, Re = 2000, $\alpha = 0°$ flow past a NACA0012 airfoil: chord-wise variation of the skin-friction coefficient.

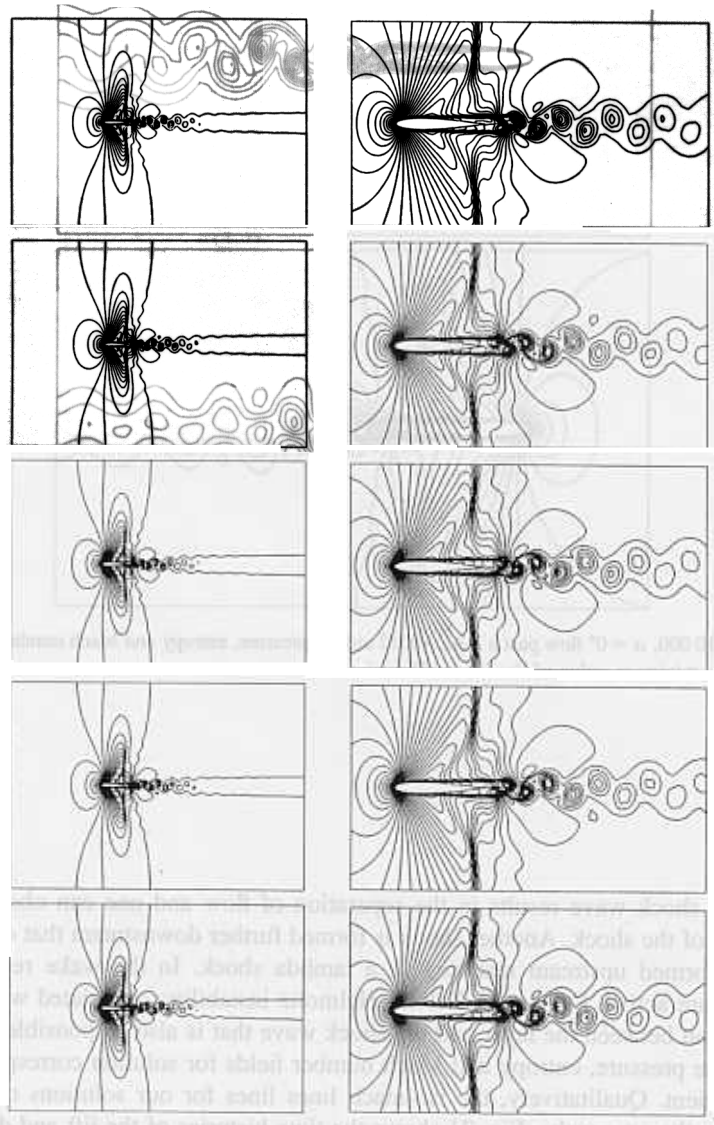

Fig. 19. Mach = 0.85, Re = 10 000, $\alpha = 0°$ flow past a NACA0012 airfoil: density field at five instants during one cycle of the lift coefficient.

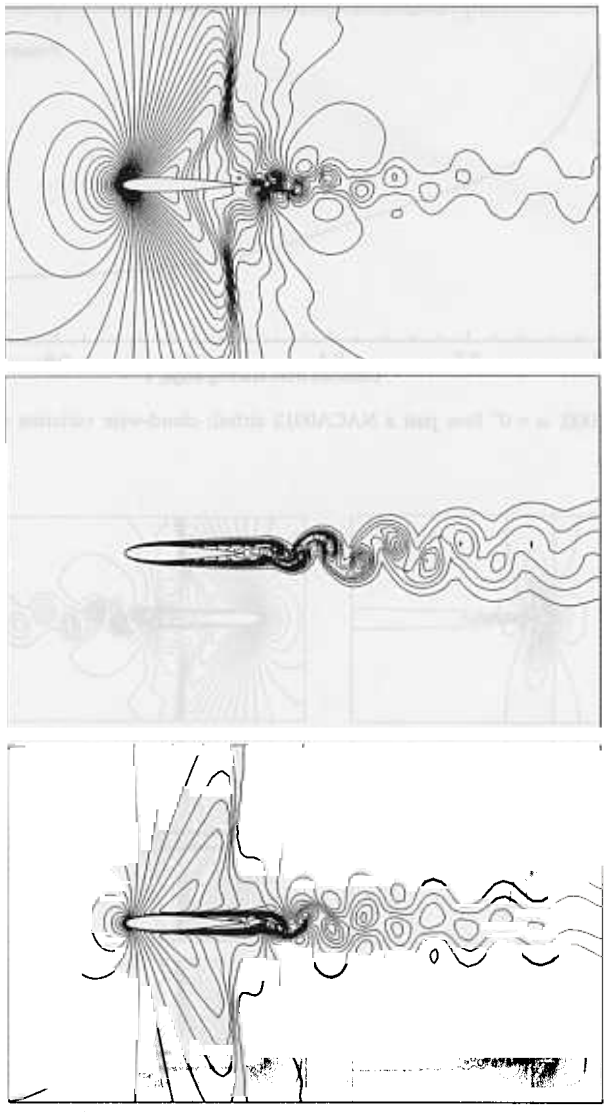

Fig. 20. Mach = 0.85, Re = 10 000, $\alpha = 0°$ flow past a NACA0012 airfoil: pressure, entropy and Mach number fields (top to bottom) for the solution corresponding to the minimum value of the lift coefficient.

boundary layer and the shock wave results in the separation of flow and one can observe the formation of a shear layer downstream of the shock. Another shock is formed further downstream that combines with the shock and expansion waves formed upstream resulting in a lambda shock. In the wake region two kinds of flow instability mechanisms are active. One is the Kelvin–Helmoltz instability, associated with the shear layers, and the other is the interaction between the layer and the shock wave that is also responsible for transonic buffeting. Shown in Fig. 20 are the pressure, entropy and Mach number fields for solution corresponding to the minimum value of the lift coefficient. Qualitatively, the iso-mach lines lines for our solutions compare quite well with those reported in [34] in the near-wake. Fig. 21 shows the time histories of the lift and drag coefficients for this computation. The Strouhal number corresponding to the lift coefficient variation is 1.58. It can be observed that

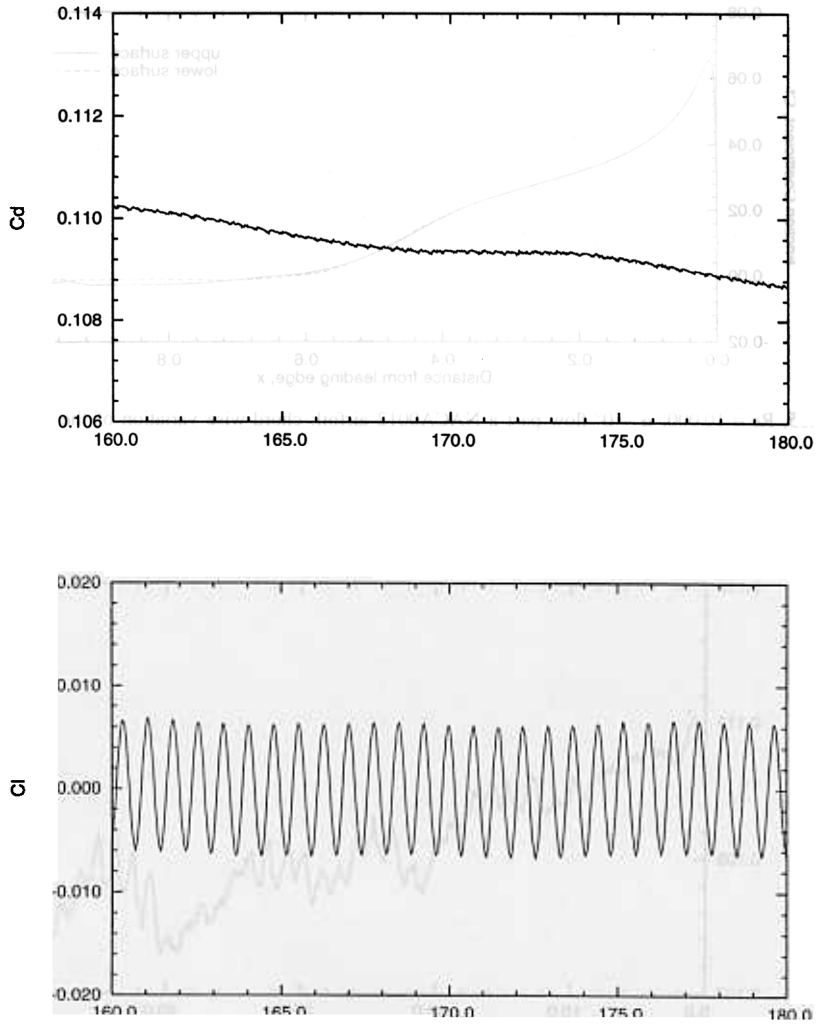

Fig. 21. Mach = 0.85, Re = 10 000, $\alpha = 0°$ flow past a NACA0012 airfoil: time histories of the lift and drag coefficients.

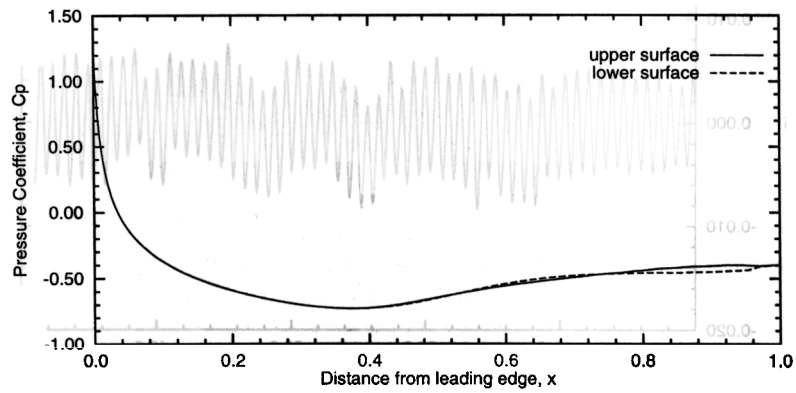

Fig. 22. Mach = 0.85, Re = 10 000, $\alpha = 0°$ flow past a NACA0012 airfoil: chord-wise variation of the pressure coefficient.

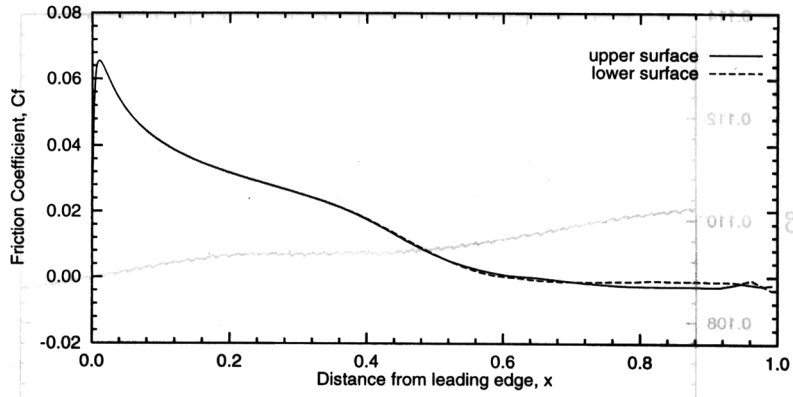

Fig. 23. Mach = 0.85, Re = 10 000, $\alpha = 0°$ flow past a NACA0012 airfoil: chord-wise variation of the skin-friction coefficient.

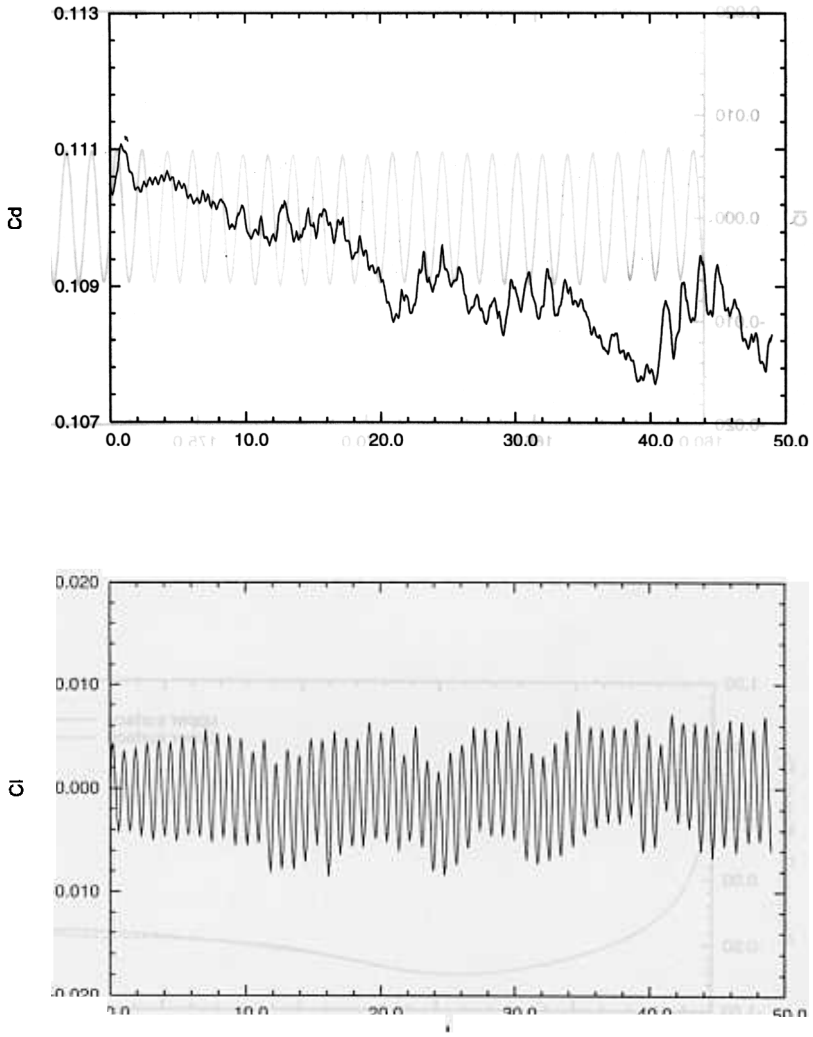

Fig. 24. Mach = 0.85, Re = 10 000, $\alpha = 0°$ flow past a NACA0012 airfoil computed with the inconsistent definition of the shock-capturing operator: time histories of the lift and drag c

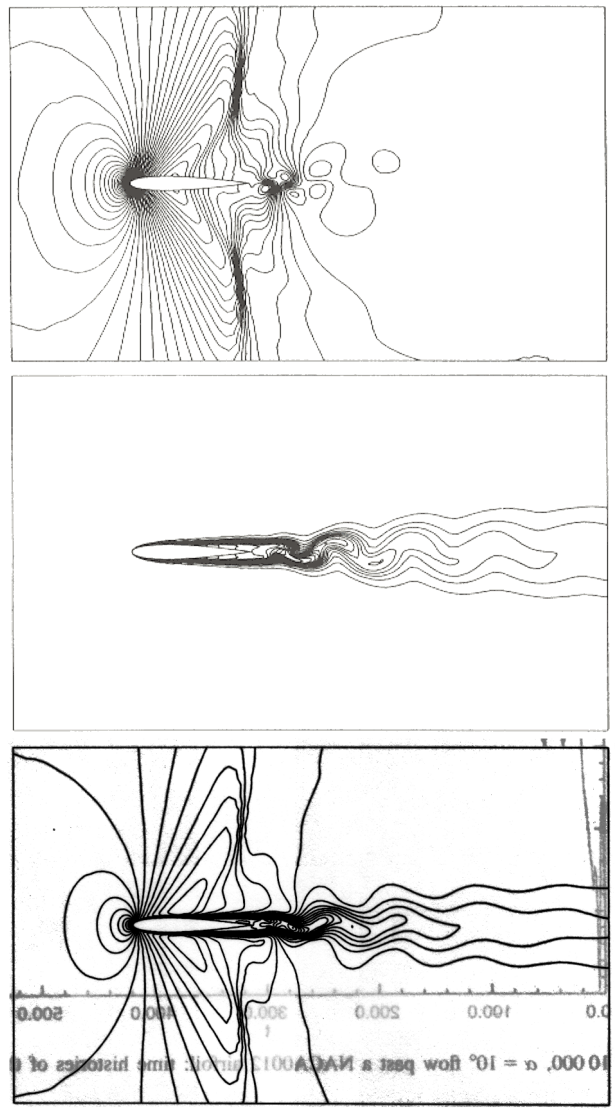

Fig. 25. Mach = 0.85, Re = 10 000, $\alpha = 0°$ flow past a NACA0012 airfoil computed with the inconsistent definition of the shock-capturing operator: pressure, entropy and Mach number fields (top to bottom) for the solution corresponding to the minimum value of the lift coefficient.

the vortices are shed from both, the upper and the lower surfaces of the airfoil. Shown in Figs. 22 and 23 are the chord-wise distribution of the pressure and skin friction coefficients for the solution corresponding to the minimum value of the lift coefficient from the computations.

To see the effect of the unsteady term in the definition of the coefficient δ in the shock capturing operator (see Eq. (26)) we continued our computations with the alternate definition of δ that does not include the unsteady term. Fig. 24 shows the time histories of the lift and drag coefficients for this segment of the computation. The flow field corresponding to the minimum value of the lift coefficient is shown in Fig. 25. When we compare Figs. 20 and 25 we observe that the two solutions look quite similar except in the regions where there is significant temporal variation. The definition of δ that excludes the unsteady term (and is therefore inconsistent) results in overly damped solutions.

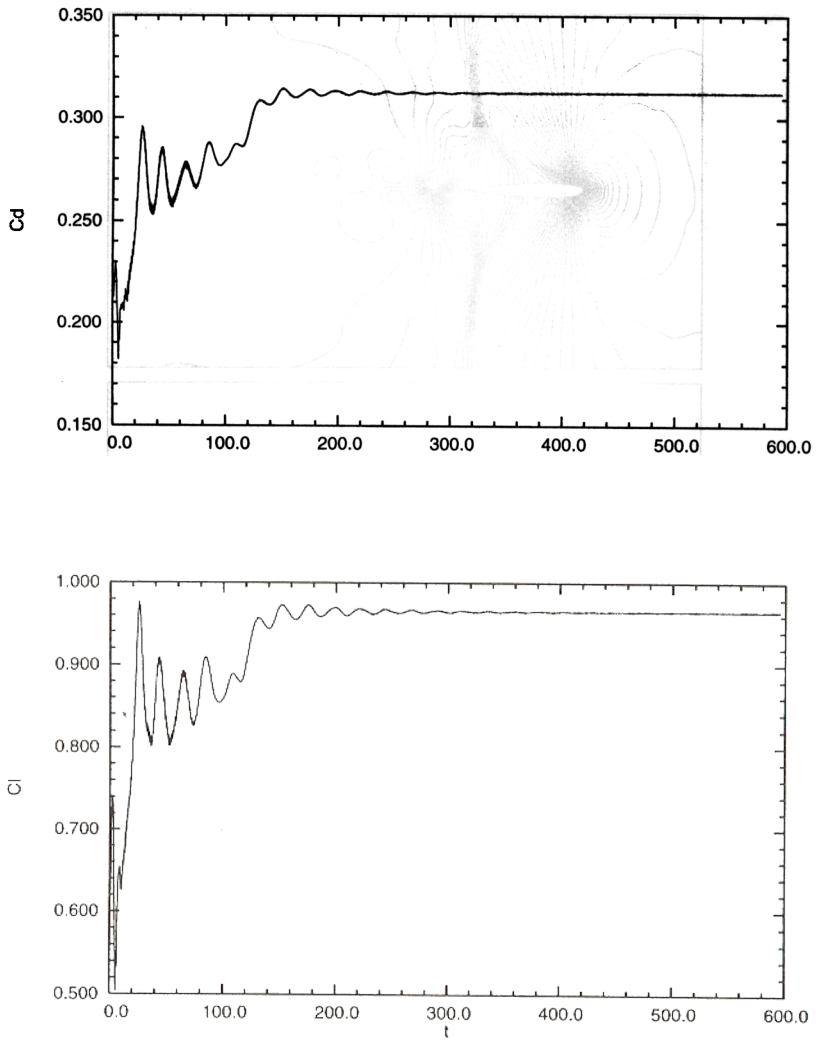

Fig. 26. Mach = 0.85, Re = 10 000, $\alpha = 10°$ flow past a NACA0012 airfoil: time histories of the lift and drag coefficients.

4.4.4. Re = 10 000, $\alpha = 10°$

In this case, the airfoil is placed in the flow at a 10° incidence to the free-stream. Our computations for this case lead to quite interesting observations. In the early phase of the computations, one observes the development of a vortex street in the wake of the airfoil along with the shock and expansion waves, the structure of which are quite similar to the ones seen in the previous case. As the computations go further we observe that the expansion fan on the upper surface of the airfoil becomes stronger. This leads to a favorable pressure gradient and therefore the flow separation is suppressed. Eventually, the unsteadiness in the flow disappears and our computations converge to a steady solution. This sequence of events can also be observed from the time histories of the lift and drag coefficients that are shown in Fig. 26. This observation is in quite contrast to what one sees for incompressible flows. In the case of incompressible flows it has been observed [3] that the unsteadiness of the flow increases as the angle of attack of the airfoil increases. The present computation is an example of a case where the compressibility effects stabilize the flow. Our preliminary computations indicate that this is an effect of the interaction of the shock waves and lateral boundaries. When the lateral boundaries are moved farther away from the airfoil, such that the shock waves do not get reflected from the side walls, regular

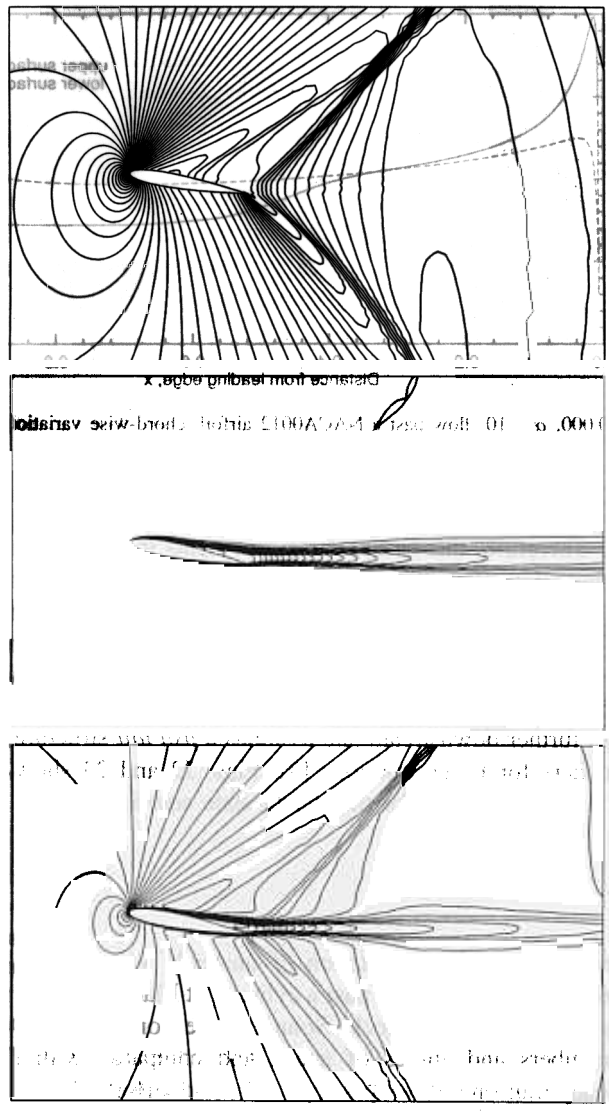

Fig. 27. Mach = 0.85, Re = 10 000, $\alpha = 10°$ flow past a NACA0012 airfoil: pressure, entropy, and Mach number fields (top to bottom) for the steady state solution.

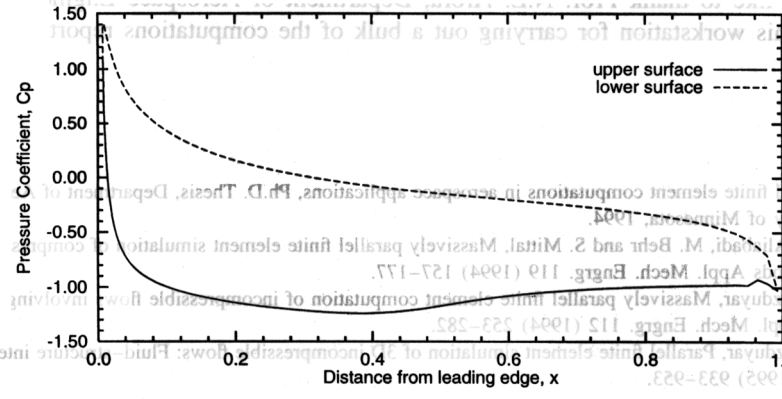

Fig. 28. Mach = 0.85, Re = 10 000, $\alpha = 10°$ flow past a NACA0012 airfoil: chord-wise variation of the pressure coefficient.

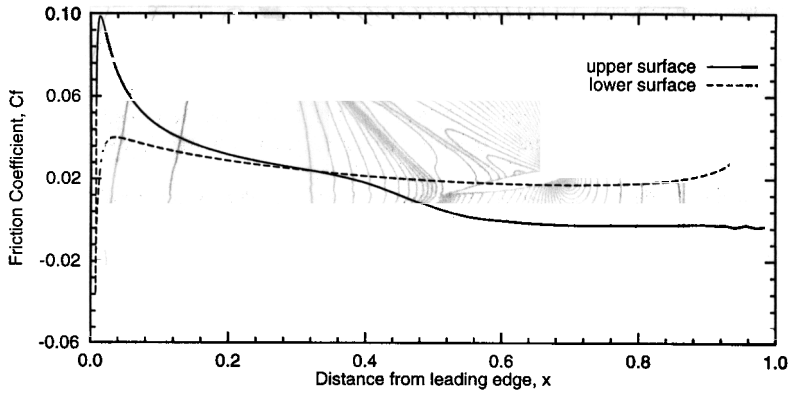

Fig. 29. Mach = 0.85, Re = 10 000, $\alpha = 10°$ flow past a NACA0012 airfoil: chord-wise variation of the skin-friction coefficient.

vortex shedding is observed. Therefore, this computation represents the simulation of flow past an airfoil in a wind-tunnel or a channel whose lateral walls are, each, 4.25 chord-lengths from the mid-chord point of the airfoil. More computations at various other angles of attacks are being currently carried out and will be presented in greater details in a later article. We have also observed the existence of multiple solutions for certain angle of attack of the airfoil to the flow. Fig. 27 shows the pressure, entropy and Mach number fields for solution corresponding to the steady-state. When we compare this figure to Fig. 20 we observe that for the $\alpha = 10°$ case the shock moves further downstream and assumes a *fish tail* structure, which is quite similar to the one reported by other researchers for Euler solutions [8]. Figs. 22 and 23 show, respectively, the chordwise distribution of the pressure and skin-friction for the steady-state solution.

5. Conclusions

We have presented our results for the computation of unsteady viscous transonic flows past airfoils and circular cylinders. The results for supersonic flow past a cylinder at Mach 2 are compared with experimental and analytical results, especially in the zone of shock. Solutions are computed for flows past airfoil at various Reynolds numbers, Mach numbers and angles of attack and compared with numerical results from other researchers. Results for unsteady transonic flows past cylinders and airfoils show interesting flow patterns and a complex interaction between the boundary/shear layers and shock/expansion waves.

Acknowledgment

The author would like to thank Prof. N.L. Arora, Department of Aerospace Engineering, IIT Kanpur, for providing access to his workstation for carrying out a bulk of the computations reported in this article.

References

[1] S.K. Aliabadi, Parallel finite element computations in aerospace applications, Ph.D. Thesis, Department of Aerospace Engineering and Mechanics, University of Minnesota, 1994.

[2] T.E. Tezduyar, S.K. Aliabadi, M. Behr and S. Mittal, Massively parallel finite element simulation of compressible and incompressible flows, Comput. Methods Appl. Mech. Engrg. 119 (1994) 157–177.

[3] S. Mittal and T.E. Tezduyar, Massively parallel finite element computation of incompressible flows involving fluid-body interactions, Comput. Methods Appl. Mech. Engrg. 112 (1994) 253–282.

[4] S. Mittal and T.E. Tezduyar, Parallel finite element simulation of 3D incompressible flows: Fluid–structure interactions, Int. J. Numer. Methods Fluids 21 (1995) 933–953.

[5] H. Schlichting, Boundary-Layer Theory, 7th edition (McGraw-Hill, New York, 1979).
[6] A.M. Kuethe and C.Y. Chow, Foundations of Aerodynamics. Bases of Aerodynamic Design (John Wley and Sons, New York, 1932).
[7] T.J.R. Hughes and T.E. Tezduyar, Finite element methods for first-order hyperbolic systems with particular emphasis on the compressible Euler equations, Comput. Methods Appl. Mech. Engrg. 45 (1984) 217–284.
[8] M.O. Bristeau, O. Pironneau, R. Glowinski, J. Periaux, P. Perrier and G. Poirier, On the numerical solution of nonlinear problems in fluid dynamics by least squares and finite element methods (II). Application to transonic flow situations, Comput. Methods Appl. Mech. Engrg. 51 (1985) 363–394.
[9] R. Lohner, K. Morgan and O.C. Zienkiewicz, An adaptive finite element procedue for compressible high speed flows, Comput. Appl. Mech. Engrg. 51 (1985) 441–465.
[10] G.J. Le Beau, The finite element computation of compressible flows, Master's Thesis, Aerospace Engineering, University of Minnesota, 1990.
[11] G.J. Le Beau and T.E. Tezduyar, Finite element computation of compressible flows with the SUPG formulation, in: M.N. Dhaubhadel, M.S. Engelman and J.N. Reddy, eds., Advances in Finite Element Analyis in Fluid Dynamics, FED-Vol. 123. ASME (New York, 1991) 21–27.
[12] T.E. Tezduyar and T.J.R. Hughes, Finite element formulations for convection dominated flows with particular emphasis on the compressible. Euler equations, in: Proc. AIAA 21st Aerospace Sciences Meeting, AIAA Paper 83-0125, Reno, Nevada, 1983.
[13] J. Peraire, J. Peiro and K. Morgan, Finite element multigrid solution of Euler flows past installed aero-engines, Comput. Mech. 11 (1993) 433–451.
[14] M.O. Bristeau, R. Glowinski, J. Periaux and H. Viviand, GAMM-workshop: Numerical simulation of compressible Navier–Stokes flows; Presentation of problems and discussion of results, in: M. Deville, ed., Proc. Seventh GAMM-Conference on Numerical Methods in Fluid Mechanics, Vol. 20 of Notes on Numerical Fluid Mechanics, (Vieweg, Wiesbaden, 1988) 442–450.
[15] S. Bovin and M. Fortin, A new artificial viscosity method for compressible viscous flow simulations by FEM, Int. J. Comput. Fluid Dyn. 1 (1993) 25–41.
[16] S.K. Aliabadi and T.E. Tezduyar, Space–time finite element computation of compressible flows involving moving boundaries and interfaces, Comput. Methods Appl. Mech. Engrg. 107(1-2) (1993) 209–224.
[17] T.J.R. Hughes and A.N. Brooks, A multi-dimensional upwind scheme with no crosswind diffusion, in: T.J.R. Hughes, ed., Finite Element Methods for Convection Dominated Flows, AMD-Vol. 34 (ASME, New York, 1979) 19–35.
[18] T.E. Tezduyar and T.J.R. Hughes, Development of time-accurate finite element techniques for first-order hyperbolic systems with particular emphasis on the compressible Euler equations, Report prepared under NASA-Ames University Consortium Interchange, No. NCA2-OR745-104, 1982.
[19] V. Venkatakrishnan, Viscous computations using a direct solver, Comput. Fluids 18(2) (1990) 191–204.
[20] T.J.R. Hughes and M. Mallet, A new finite element formulation for computational fluid dynamics: IV. A discontinuity-capturing operator for multidimensional advective–diffusive systems, Comput. Methods Appl. Mech. Engrg. 58 (1986) 329–339.
[21] F. Shakib, Finite element analysis of the compressible Euler and Navier–Stokes equations, Ph.D. Thesis, Department of Mechanical Engineering, Stanford University, 1988.
[22] T.E. Tezduyar, S. Mittal, S.E. Ray and R. Shih, Incompressible flow computations with stabilized biliner and linear equal-order-interpolation velocity–pressure elements, Comput. Methods Appl. Mech. Engrg. 95 (1992) 221–242.
[23] S.K. Aliabadi, S.E. Ray and T.E. Tezduyar, SUPG finite element computation of compressible flows with entropy and conservation variables formulations, Comput. Mech. 11 (1993) 300–312.
[24] Y. Saad and M. Schultz, GMRES: A generalized minimal residual algorithm for solving nonsymmetric linear systems. SIAM J. Sci. Statis. Comput. 7 (1986) 856–869.
[25] A.H. Shapiro, The Dynamics and Thermodynamics of Compressible Fluid Flows (John Wiley and Sons, New York, 1958).
[26] H.W. Liepmann and A. Roshko, Elements of Gas Dynamics (John Wiley and Sons, Inc., New York, 1957).
[27] J. Oliger and A. Sundstrom, Theoretical and practical aspects of some initial boundary value problems in fluid dynamics, SIAM J. Appl. Math. 35 (1978) 419–446.
[28] B. Gustafsson and A. Sundstrom, Incompletely parabolic problems in fluid dynamics, SIAM J. Appl. Math. 35 (1978) 343–357.
[29] M. Van Dyke. An Album of Fluid Motion (Parabolic Press, Stanford, CA, 1982).
[30] M. Behr, Stabilized finite element methods for incompressible flows with emphasis on moving boundaries and interfaces, Ph.D. Thesis, Department of Aerospace Engineering, University of Minnesota, 1992.
[31] M.O. Bristeau, R. Glowinski, J. Periaux and H. Viviand, Presentation of problems and discussion of results, in: M.O. Bristeau, R. Glowinski, J. Periaux and H. Viviand, eds., Numerical Simulation of Compressible Navier–Stokes Flows, Vol. 18 of Notes on Numerical Fluid Mechanics (Vieweg, Wiesbaden, 1987) 1–40.
[32] B. Muller, T. Berglind and A. Rizzi, Implict central difference simulation of compressible Navier–Stokes flow over a NACA 0012 airfoil, in: M.O. Bristeau, R. Glowinski, J. Periaux and H. Viviand, eds., Numerical Simulation of Compressible Navier–Stokes Flows, Vol. 18 of Notes on Numerical Fluid Mechanics (Vieweg, Wiesbaden, 1987).
[33] F. Shakib, T.J.R. Hughes and Z. Johan, A multi element group preconditioned GMRES algorithm for non-symmetric systems arising in finite element analysis, Comput. Methods Appl. Mech. Engrg. 75 (1989) 451–456.
[34] L. Cambier, Computation of viscous transonic flows using an unsteady type method and a zonal grid refinement technique, in: M.O. Bristeau, R. Glowinski, J. Periaux and H. Viviand, eds., Numerical Simulation of Compressible Navier–Stokes Flows, Vol. 18 of Notes of Numerical Fluid Mechanics (Vieweg, Wiesbaden, 1987).
[35] N. Satofuka, K. Morinishi and Y. Nishida, Numerical solution of two-dimensional compressible Navier–Stokes equations using rational Runge–Kutta method, in: M.O. Bristeau, R. Glowinski, J. Periaux and H. Viviand, eds., Numerical Simulation of Compressible Navier–Stokes Flows, Vol. 18 of Notes on Numerical Fluid Mechanics (Vieweg, Wiesbaden, 1987).